Supplementary material

Biomass pyrolysis with Fe-Ni-CaO char-based catalyst for efficient green hydrogen generation and bio-oil upgrading via coupled C–H/O–H activation

Qiuxiang Lu[1], Yao Wang[1], Qi Cao, Gang Wu, Huiyan Zhang*

Key Laboratory of Energy Thermal Conversion and Control of Ministry of Education, School of Energy and Environment, Southeast University, Nanjing 210096, PR China

[1] These two authors contributed equally to the work.

[*] Corresponding author: *Huiyan Zhang (H.Z.)*.

E-mail address: hyzhang@seu.edu.cn

The PDF file includes:

Supplementary Text

Figs. S1 to S20

Tables S1 to S3

Supplementary Text

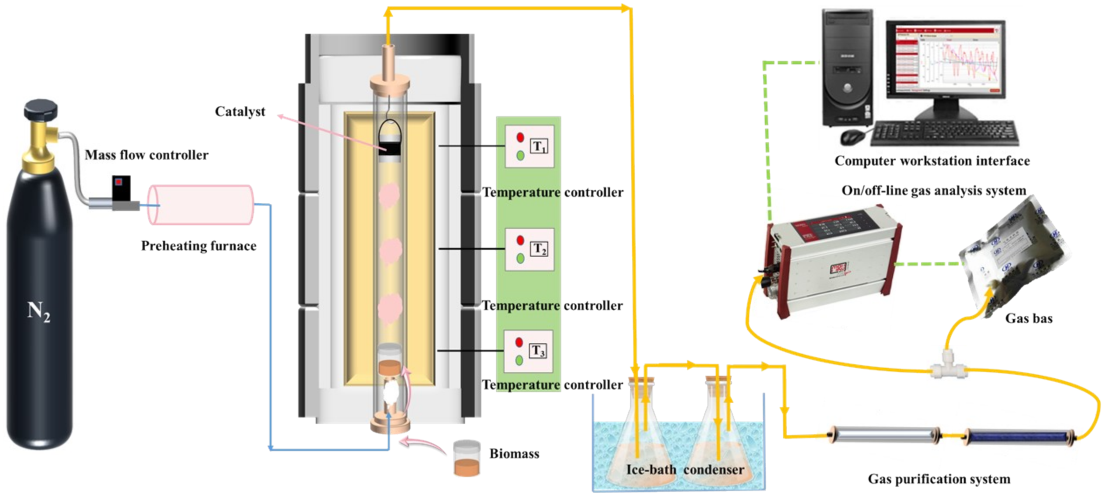

Supplementary Fig. 1. Schematic diagram of catalytic reforming of biomass pyrolysis tar to hydrogen.

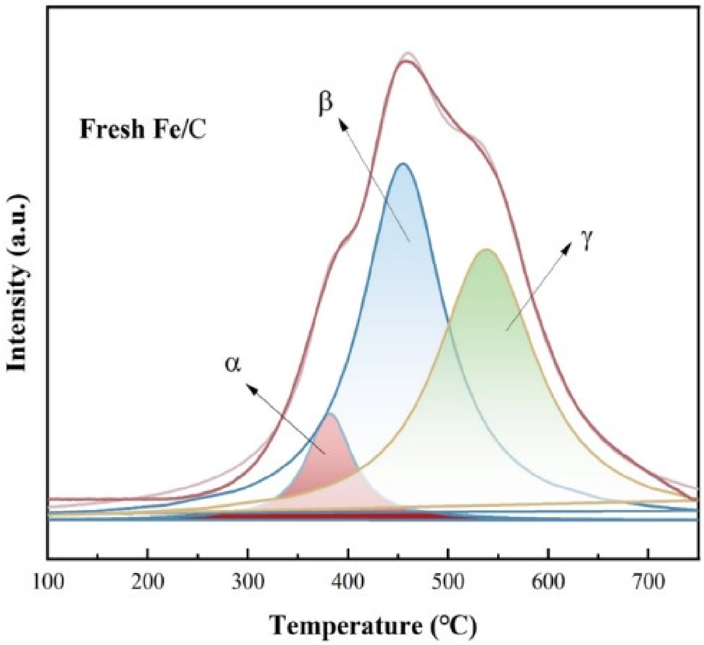

Supplementary Fig. 2. Reduction characteristics of the catalyst (H_2-TPR of fresh Fe/C, which shows three reduction peaks, Fe_2O_3→Fe_3O_4→FeO→Fe).

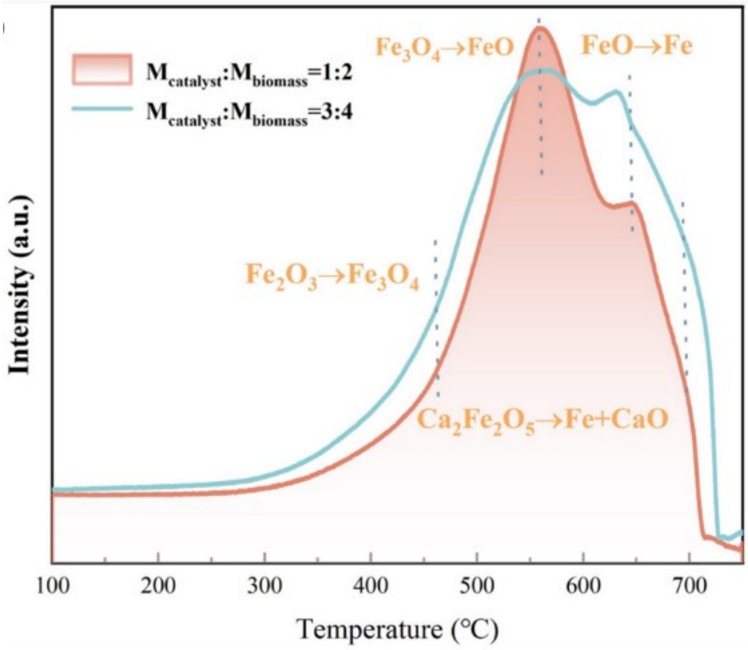

Supplementary Fig. 3. Reduction characteristics of the spent Fe/C catalyst.

As can be seen in Fig. 3, changing the ratio of catalyst to biomass has little effect on the peak shape of the reduction peak, the difference being that increasing the amount of catalyst results in a flatter positional curve of the reduction peak, which can be attributed to the high content of +2 and +3 valent iron in the catalyst.

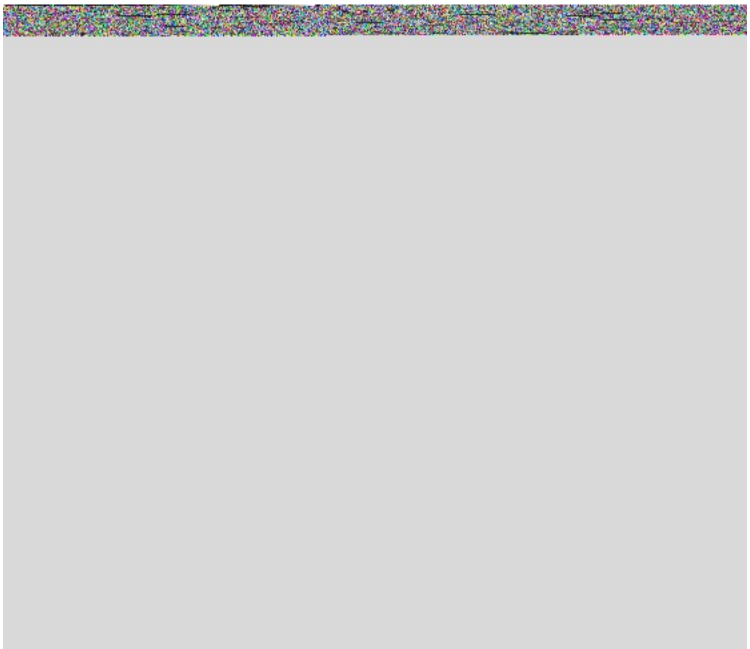

Supplementary Fig. 4. Reduction characteristics of the spent Fe/C catalyst.

From the Fig. 4, it can be seen that when the ratio of catalyst to biomass is 3:4, the position curves of the first and second reduction peaks are flatter, which can be attributed to the higher content of Fe_3O_4 in the catalyst. Again, the third reduction peak has an earlier reduction temperature and a sharp peak shape, which indicates that there is less iron content in the +2, which is rapidly reduced in a short period of time. Meanwhile, the curve of the last hydrogen reduction peak is also flat, which is attributed to the presence of a large amount of Fe-Ca compounds in the catalyst. The peak shape of the hydrogen reduction peak when the mass ratio of the two is 1:2 is sharper showing a volcano shape and the temperature range of the reduction curve is narrower, which indicates that the valence of iron species in this catalyst is concentrated in +2 and +3.

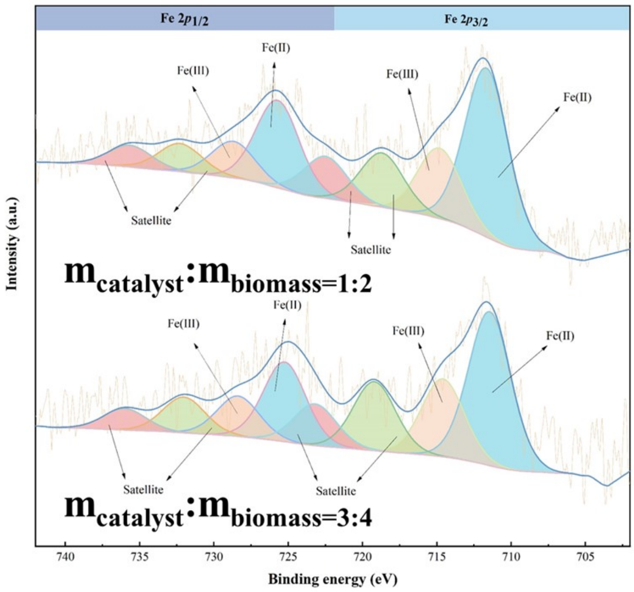

Supplementary Fig. 5. Fe 2*p* evolution of spent Fe-CaO/C catalyst.

In Fe 2*p* spectra, the peaks at 710.8 and 726.4 eV, 715.2 and 727.9 eV were marked as 2 $p_{3/2}$ and 2 $p_{1/2}$ of Fe^{2+} and Fe^{3+}, respectively.

Supplementary Fig. 6. Ca 2*p* evolution of spent Fe-CaO/C catalyst

In Ca 2*p* spectra, around 351 eV and 347 eV are Ca 2*p*1/2 and Ca 2*p*3/2, respectively.

Supplementary Fig. 7. O 1*s* evolution of spent Fe-CaO/C catalyst.

The O 1s was fitted to the peaks of lattice O (O_L), oxygen vacancy (O_V) and O-H bond by Gaussian functions. The calculation of the relative content of each oxygen species was determined by area integration. The addition of mass ratio (1:2→3:4) the Ov concentration decreases (78.00%→66.32%).

Supplementary Fig. 8. C 1s evolution of spent Fe-CaO/C catalyst.

The high-resolution C 1s spectra can be assign to C-C, C-C and C-O bonds at 284.2, 285.4 and 288.6 eV, respectively.

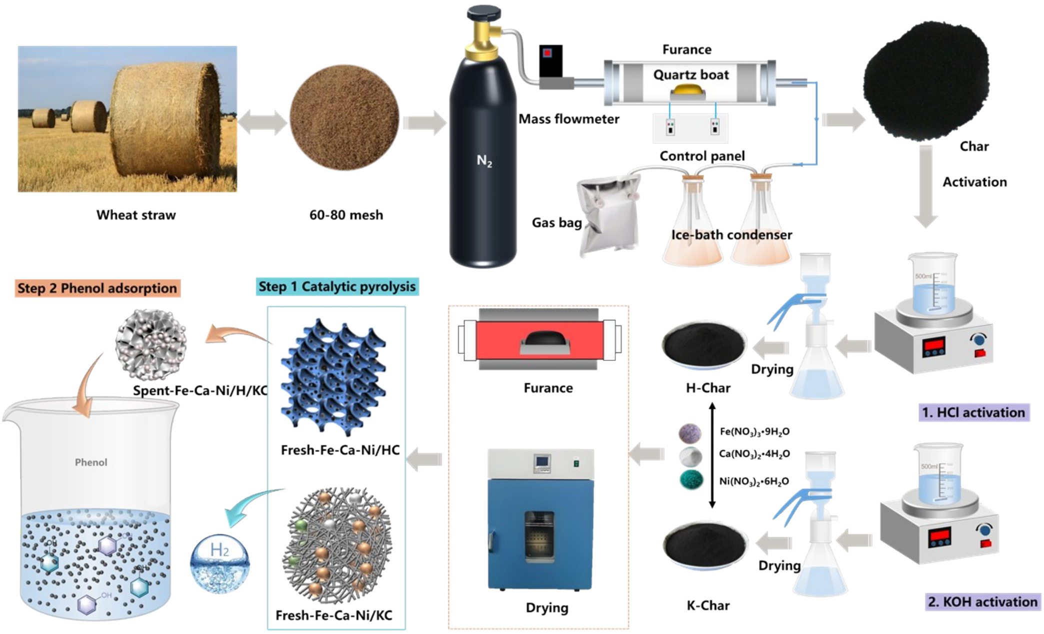

Supplementary Fig. 9. Schematic of the preparation process of bio-char and the preparation of catalyst.

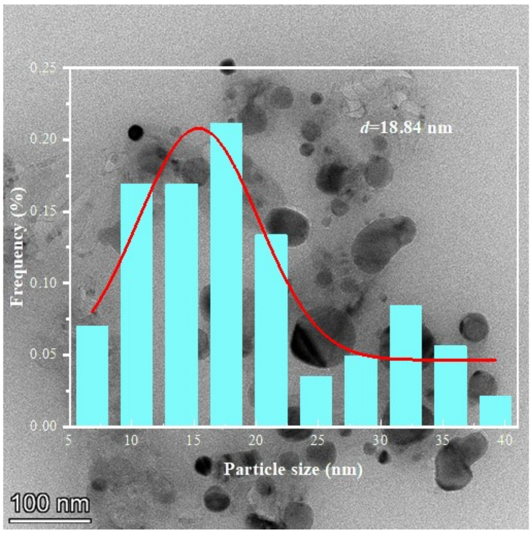

Supplementary Fig. 10. Morphology characterizations and particle dimension frequency of the fresh catalysts Fe-CaO-Ni/0.2HC fresh catalyst.

The smaller, darker particles represent the active component metal oxides, while the larger, lighter blocks represent the alloy. The average particle size of the Fe-CaO-Ni/0.2HC catalyst is 18.84 nm.

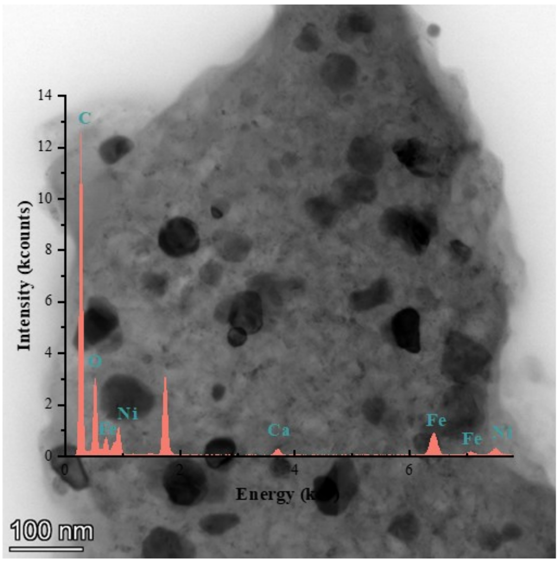

Supplementary Fig. 11. surface characterizations and element distribution of the fresh catalysts Fe-CaO-Ni/0.2HC fresh catalyst.

The EDX results show that the catalyst surface contains mainly Fe, Ni, Ca, C and O, with no other heterogeneous elements.

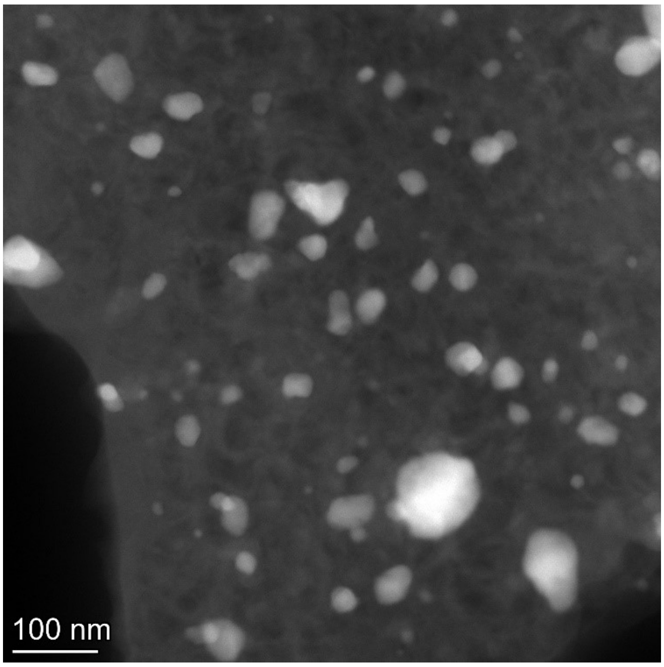

Supplementary Fig. 12. TEM dark field image of fresh catalysts Fe-CaO-Ni/0.2HC fresh catalyst.

The smaller particles represent the active component metal oxides, while the larger blocks represent the alloy.

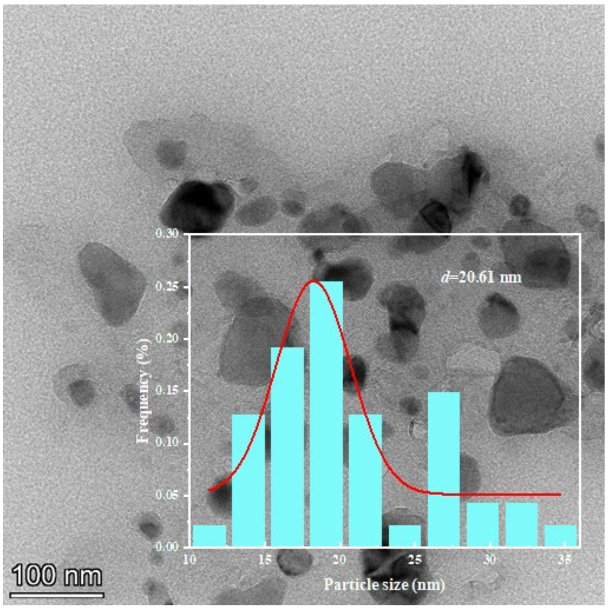

Supplementary Fig. 13. Morphology characterizations and particle dimension frequency of the fresh Fe-CaO-Ni/0.3KC fresh catalyst.

Cube-shaped thin layers outside particles are clearly observed on catalyst surface. The average particle size of Fe-CaO-Ni/0.3KC catalyst is 20.61nm, larger than those in Fe-CaO-Ni/O.2HC.

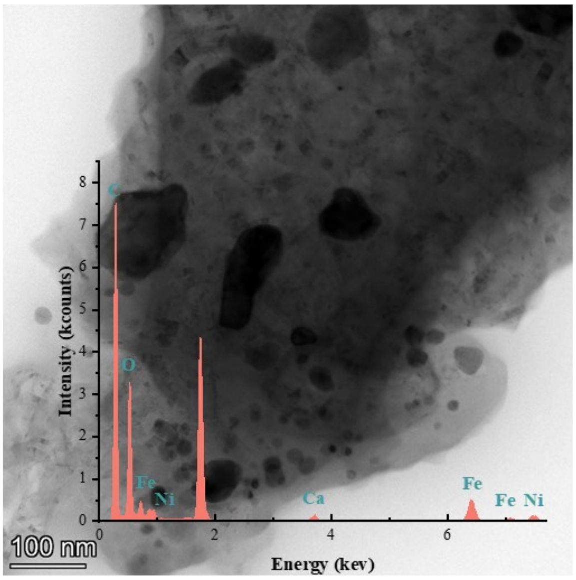

Supplementary Fig. 14. surface characterizations and element distribution of the fresh Fe-CaO-Ni /0.3KC fresh catalyst.

Cube-shaped thin layers outside particles are clearly observed on catalyst surface. The EDX results show that the catalyst surface contains mainly Fe, Ni, Ca, C and O, with no other heterogeneous elements.

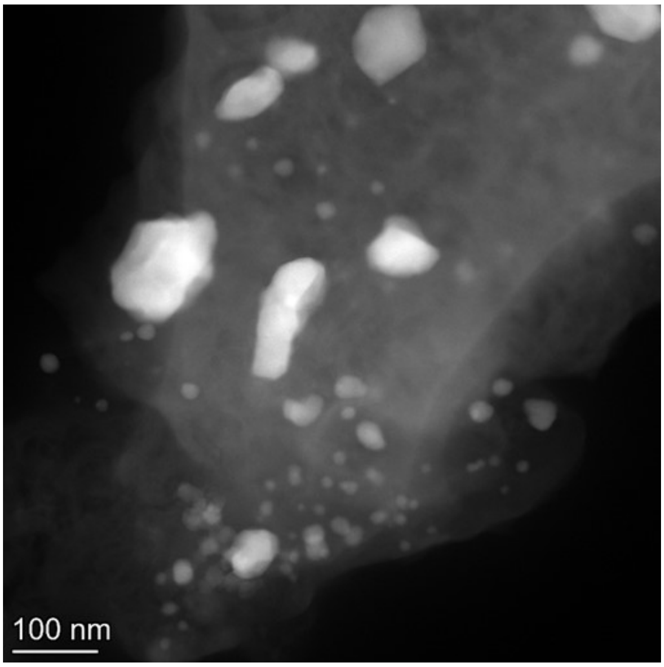

Supplementary Fig. 15. TEM dark field image of fresh catalysts Fe-CaO-Ni/0.2HC fresh Fe-CaO-Ni/0.3KC.

Cube-shaped thin layers outside particles are clearly observed on catalyst surface.

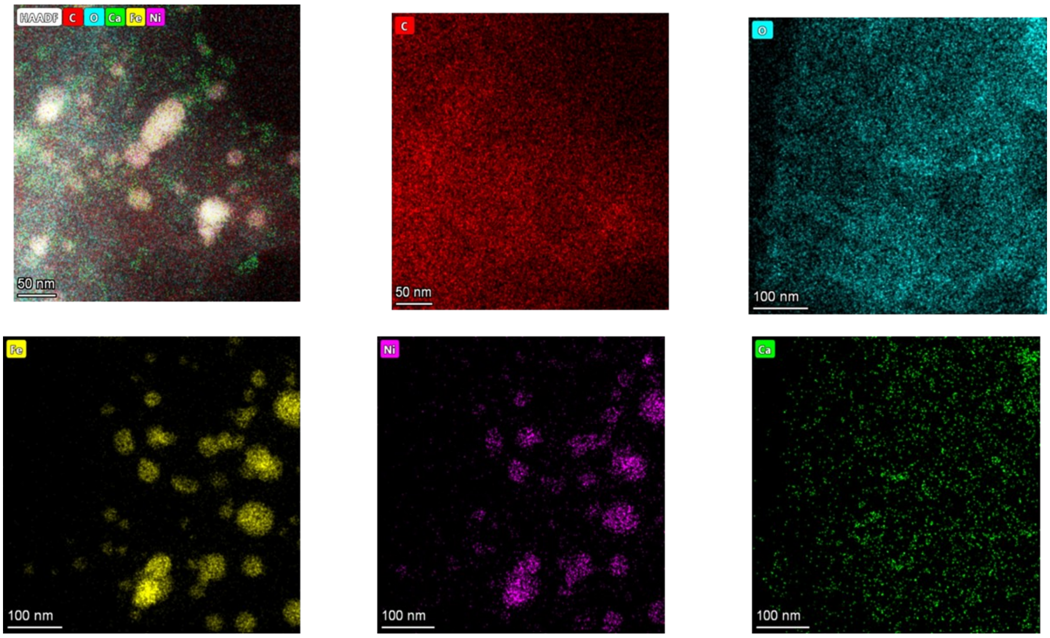

Supplementary Fig. 16. elemental mapping images of fresh catalysts Fe-CaO-Ni/0.3KC.

C, O, Fe, Ni and Ca can be observed in the TEM mapping diagram, where the positions of Fe and Ni overlap.

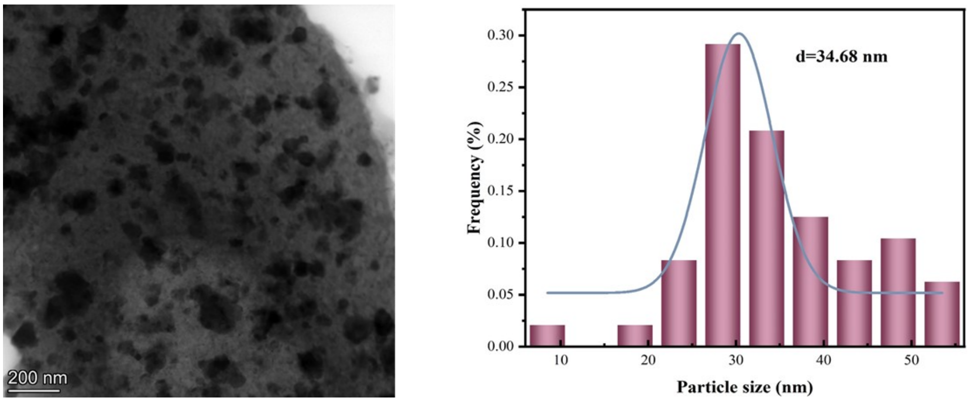

Supplementary Fig. 17. TEM image and particle distribution of spent Fe-CaO-Ni/0.2HC.

Dark black particles and carbon film can be seen in TEM image, and the particle size statistics of the particles in the figure yielded that the size of the particles was 34.68 nm, which was larger than that of the fresh catalyst particles.

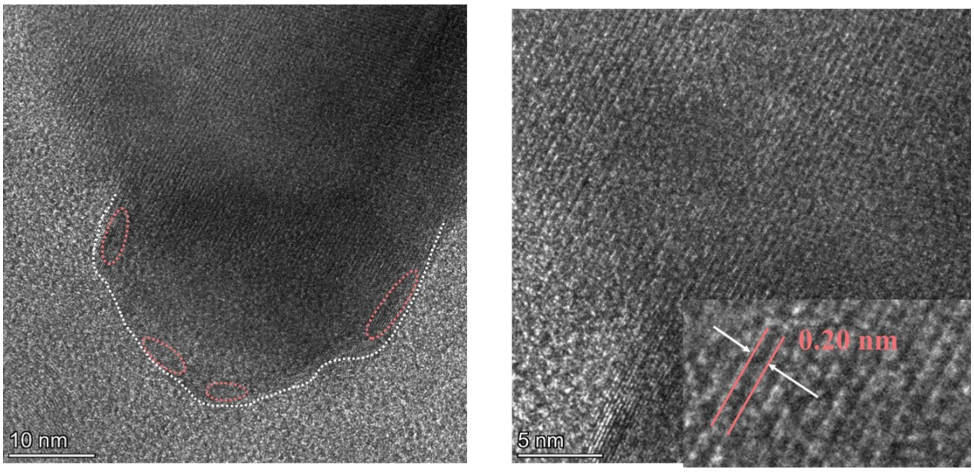

Supplementary Fig. 18. High-resolution TEM of spent Fe-CaO-Ni/0.3KC.

The presence of carbon cladding with ordered carbon streaks was also confirmed in the high-resolution TEM images.

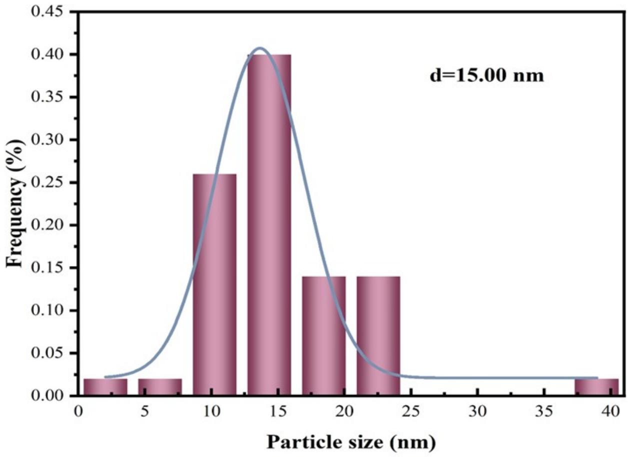

Supplementary Fig. 19. Particle distribution of spent Fe-CaO-Ni/0.3KC.

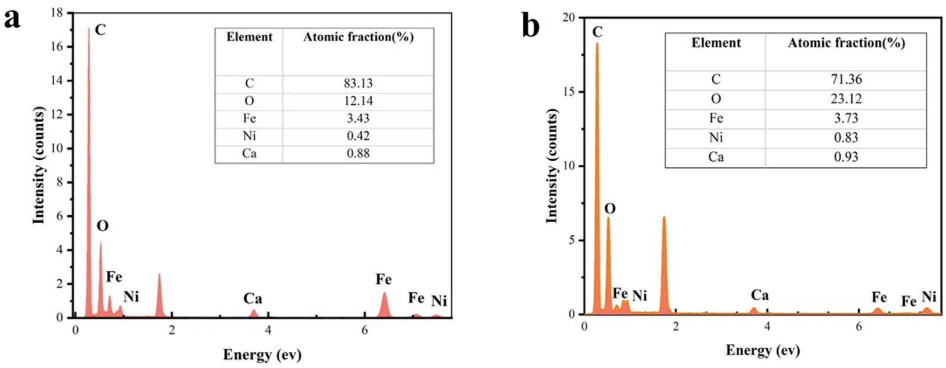

Fig. 20. Composition and content of elements in the spent carrier-modified catalyst (a: Fe-CaO-Ni/0.2HC; b Fe-CaO-Ni/0.3KC).

Table S1. Proximate and ultimate analyses of the WS.

Proximate analysis (wt%, d)				Ultimate analysis (wt%, daf)				
	VM	A	FC	C	H	O[a]	N	S
WS	83.62	8.44	7.94	47.34	7.13	44.35	1.02	0.16
H-WS	79.84	3.72	16.44	51.72	6.49	40.59	1.13	0.07

VM: volatile matter; A: ash; FC: fixed carbon; d: dry basis; daf: dry ash free basis. a: By difference.

Table S2. Biomass pyrolysis product distribution in the 500-800 °C temperature range.

	Y_{HO} (in wt% of biomass, daf)	Y_{Gas} (in wt% of biomass, daf)	Y_{Char} (in wt% of biomass, daf)	Y_{LO+W} (in wt% of biomass, daf)
600 °C	4.94	29.73	27.93	37.40
700 °C	4.06	32.78	27.96	35.20
800 °C	1.71	34.00	27.99	36.30

Table S3. Textural properties of the catalysts.

Catalyst	Surface Area （m^2/g）	Pore Volume （cm^2/g）	Average pore diameter （nm）
Fresh Fe-Ni-Ca/0.2HC	727.80	0.599	3.17
Fresh Fe-Ni-Ca/0.3KC	904.62	0.598	2.64
Spent Fe-Ni-Ca/0.3KC	269.62	0.233	3.45
Bio-char	235.77	0.159	2.70
AC	947.38	0.515	2.26

Table S4. Comparison of this work with relevant research on hydrogen yield and key reaction conditions.

Feedstock	Temperature (°C)	Catalyst	Hydrogen content (mL/g)	Ref.
Hemicellulose	800	-	136.42	1
Biomass tar	900	Ni-Fe/ASA@HZSM-5	110.5	2
Wheat straw	750	Fe/Char	81.39	3
Wheat straw	650	Ni–Co–Mn	59.58	4
Biomass	923	$CaCO_3$	308	5
Chinese herb residues	700	K–Fe	135.36	6
Pine sawdust	600	Ni-Ce/C9A3(AN-CF)	294.31	7
Wheat straw	600	Fe-Ni-Ca/Char	345	**This work**

References:

1. G. Chen, W. Du, J. Cai, J. Li, J. Tao, M. Irfan Rajput, B. Yan, Z. Wang, *Applications in Energy and Combustion Science*, 2025, **24**, 100381.
2. X. Li, Z. Wang, Y. Zhang, W. Zhang, H. Zhang, P. Liu, T. Lei, *Journal of Environmental Management*, 2025, **389**, 126016.
3. Y. Shi, W. Zhao, M. Tahir, E. Lora, A. N. Kozlov, M. V. Penzik, Y. Zhang, S. Zhang, *Journal of Analytical and Applied Pyrolysis*, 2026, **194**, 107539.
4. M. Xu, Z. Shi, X. Zhu, Y. Lai, A. Xia, Y. Huang, X. Jiang, J. He, M. Zhou, X.Zhu, Q. Liao, *International Journal of Hydrogen Energy*, 2024, **52**,83-96.
5. R.D. Gomez Vásquez, J. D. Rhenals-Julio, J. M. Mendoza, J.Acevedo, A. Silvera, *Applied Thermal Engineering*, 2025, **272**, 126454.
6. Y. Li, Z. Guo, H. Zhu, F. Wang, L. Lang, X. Yin, C. Wu, *International Journal of Hydrogen Energy*, 2025, **196**, 152543.
7. C. Wei, X. Zeng, X. Wang, Z. Jian, G. Hao, C. Xiao, D. Gong, *Journal of the Energy Institute*, 2025, **123**, 102328.

Table S5. ICP result of bio-char

Content (wt%)	Si	Al	Ca	Fe	K	Mg	Na
Bio-char	1.04	0.06	1.36	0.09	2.09	0.33	0.12

.